Electron-Microscope Images of the Crystal Lattice of Gold Containing Planar Defects

By Y. Takai, H. Hashimoto and H. Endoh

Department of Applied Physics, Osaka University, 2-1 Yamadaoka, Suita, Osaka 565, Japan

Abstract

Using the aberration-free focus (AFF) imaging condition in tilted illumination and by adjusting the thickness of gold crystals to optimum values, the electron-microscope images of gold atoms in perfect crystals are formed at the correct positions of atoms with a resolution higher than the theoretical resolution limit in normal operation. This method is applied to observe the images of atoms in gold crystals containing planar defects such as twin boundaries and stacking faults. The observed contrast of the images is compared with theoretical calculations based on both the Howie–Whelan theory of electron diffraction in many-beam form and an electron image-formation theory. The agreement between observations and theoretical calculations is fairly good.

1. Introduction

Recently, structure images of crystals containing twins, stacking faults and grain boundaries at the atomic level were observed for gold (Komoda, 1966; Ishida & Ichinose, 1977; Hashimoto, Sugimoto, Takai & Endoh, 1978) and silicon crystals (Krivanek & Maher, 1978; Olsen & Spence, 1979; Izui, Furuno, Nishida & Otsu, 1978–79) by using high-resolution electron microscopes. But, as was shown by Hashimoto, Endoh, Takai, Tomioka & Yokota (1978–79), intensity maxima or minima do not always appear at the positions of atoms in crystals even for perfect crystals. It is theoretically expected that the image contrast is not generally the same as for the potential projection of atoms or atom groups, when the specimen crystals are not thin enough to approximate to weak phase gratings (Boersch, 1947; Cowley, 1959) and the separation of atoms or atom groups in the unit cell is smaller than the half-width of the spread function, which is the Fourier transform of the complex transfer function of the lens. Therefore, in order to see the position of atoms in crystals from the electron-microscope images, it is necessary to compare the observed images with theoretical images which are calculated by taking into account the behaviour of electron waves in crystals and image-forming lenses. The behaviour of electron waves

in specimen crystals and image-forming lenses is well described by the dynamical theory of electron diffraction such as the Cowley–Moodie theory (O'Keefe, 1973) and the Bethe theory (Hashimoto, Kumao, Endoh, Nissen, Ono & Watanabe, 1975) and the image-formation theory (Scherzer, 1949).

It was demonstrated by Hashimoto, Endoh, Tanji, Ono & Watanabe (1977) that the periodic intensity distribution of electron waves at the bottom face of a crystal whose period is 0·5 Å could be photographed by using an electron microscope with a resolution of 2·6 Å, and adjusted to the aberration-free focus (AFF) condition in axial illumination, which eliminated the effect of spherical aberration (Hashimoto *et al.*, 1978–79). It was also demonstrated by Hashimoto, Takai, Yokota, Endoh & Fukada (1980) that the images of atoms in gold crystals of optimum thickness could be photographed at their correct position by adjusting the lens to the AFF condition in tilted illumination, which eliminates the effects not only of spherical aberration but also of chromatic aberration.

In the present paper, the Howie–Whelan theory, which is extended to the form applicable to the calculation of the electron-microscope images of atoms in crystals, is first discussed, and then the AFF condition in tilted illumination, which is not fully discussed in the previous paper (Hashimoto *et al.*, 1980), is discussed. The images of atoms in gold crystals containing twin boundaries and stacking faults are observed using the tilted-illumination AFF condition with a resolution higher than the theoretical resolution limit for normal operation of the electron microscope. It is noted that the images of atoms appeared at the correct positions of atoms by comparing with theoretical calculations.

2. Method of calculation of image contrast

In order to discuss the behaviour of electron waves in crystals, the Howie–Whelan (1961) theory extended to the many-wave case is used, but the numbers of waves used in the calculation are decreased by considering the symmetry of the excited wave (Fukuhara, 1966). The increment dV of a column vector V on passing through the slab dz, whose elements V_g are the complex

amplitudes of the diffracted waves, is given by the differential wave equation in the matrix form as

$$\frac{d\mathbf{V}}{dz} = 2\pi i [\mathbf{A} + \{\beta_g\}] \, \mathbf{V}, \tag{1}$$

where $\mathbf{A}$ is the scattering matrix, whose elements are given for the crystal with no absorption by

$$A_{00} = 0, \quad A_{gg} = s_g, \quad A_{gh} = \frac{U_{g-h}}{2K}. \tag{2}$$

The matrix $\mathbf{A}$ does not depend on the depth z measured normal to the crystal surface. s_g is the distance of the reciprocal-lattice point g of a perfect-crystal region from the reflecting sphere measured in the direction of z, U_g is the Fourier coefficient of the scattering potential, K is the electron wave vector in the crystal. $\{\beta_g\}$ is a diagonal matrix which shows the deviation of the reciprocal-lattice points of the distorted regions from the reflecting sphere and its elements are given by

$$\{\beta_g\} = \left\{ |g| \frac{dR_g}{dz} + \theta_g |g| \frac{dR_g}{dx_g} \right\}_{\text{diagonal}}, \tag{3}$$

where R_g is the component of the displacement vector $\mathbf{R}$ along g and x_g is a lateral coordinate along g. The first term on the right of (3) is due to the local angular rotation of the lattice planes, while the second takes account of the local change in the lattice spacing. In the present case, the images of twins and stacking faults whose planes are parallel to the incident beam are treated and it is assumed as the first step that there is no displacement of atoms perpendicular to the beam direction; i.e. $dR_g/dz = 0$. The second part of (3), therefore, becomes important. However, if a large distortion exists in the crystal, the column approximation using a small unit cell may not be applicable, because the interference of electron waves scattered by the atoms in the distorted region cannot be taken into account. Therefore, in the present calculation, large unit cells containing the planar defects were used as was done by Cowley (1975). In Fig. 1, the fundamental unit cell $ABCD$ and the large unit cell $A'B'C'D'$ containing a twin boundary TT' are shown by black lines. Since atom displacements around defects are already included in the large unit cell, it is not necessary to calculate the second part of (3) and hence $\{\beta_g\} = 0$. The U_g were calculated by assuming the atom arrangement around the defect. In the present calculation, small displacements of atoms around the planar defects are not included. Atomic scattering factors used in the present calculation are calculated by using the analytic expression for atomic scattering factors given by Smith & Burge (1962) and also Doyle & Turner (1968). The intensity of electron waves at the bottom face of the crystal was calculated by carrying out numerical integration of the differential equation (1)

by the Runge–Kitta method. Since a large unit cell in crystals inevitably excites a large number of diffracted waves, a large memory in the computer is needed to obtain reliable results. In order to use as many waves as possible without increasing the amount of memory, the symmetry property of crystals was used (Fukuhara, 1966) and the waves which behave in the same way in the crystal were stored in the same memory. The details of the calculation are described in the Appendix. Using this method, the number of waves included in the program could be increased seven- or eightfold for high-symmetry crystals and twice for low-symmetry crystals.

Image intensity $I(\mathbf{r})$ at the image plane of the objective lens was obtained by the square of the Fourier transform of the waves at the bottom face of the crystal which are modified by the phase-contrast transfer function of the objective lens as follows;

$$I(\mathbf{r}) = |\sum_g V_g \exp(-i\gamma_g) \exp(2\pi i \mathbf{g}\mathbf{r})|^2. \tag{4}$$

γ_g is the phase angle of the contrast transfer function (Scherzer, 1949) and is given by

$$\gamma_g = \frac{\pi}{2\lambda} [C_s \alpha_g^4 - 2\Delta f \alpha_g^2], \tag{5}$$

where λ, C_s, Δf and α_g are the electron wavelength, the spherical aberration coefficient, the amount of defocus (Δf is positive for under-focus) and the angles of the diffracted beams to the optical axis, respectively. The waves used in the calculation of (4) are those passing through the objective aperture.

3. Adjustment of crystal thickness and defocus value for obtaining the correct image of atoms

As already discussed, the electron-microscope images are the projection of the intensity distribution of electron waves at the bottom face of the crystal to the image plane. Therefore, first, it is necessary to find out the condition that the intensity maxima of the electron waves at the bottom face of the crystal appear at the
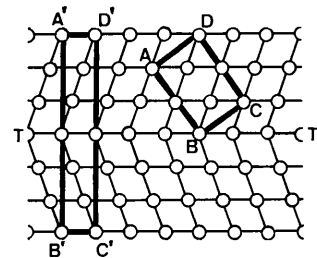

Fig. 1. Fundamental unit cell $ABCD$ and a large unit cell $A'B'C'D'$ containing a twin boundary TT'.

atom positions. As shown in Fig. 2, the amplitudes and phases of the electron waves which are Bragg reflected by the lattice planes of (000), {111} and {200} in the gold crystal in 011 orientation change with increasing crystal thickness and become the same in phase and nearly the same in amplitude at the thickness 105 Å. Since the phases of the Bragg-reflected electron waves are a function of the atom positions, it is expected that the intensity maxima of electron waves which are formed by the interference of these waves appear at the positions of atoms in the crystal. Fig. 3 shows the thickness dependence of the positions of the intensity maxima of electron waves which are formed by the interference of electron waves in two kinds of combination, i.e. three waves 000, 1$\bar{1}$1, $\bar{1}$11 and four waves 000, 200, 11$\bar{1}$, 1$\bar{1}$1. The crystal is in the 01$\bar{1}$ orientation and the incident electron wave is parallel to [01$\bar{1}$]. As can be seen in Fig. 3, the intensity maxima appear at the atom positions when the thickness is 105 ± 5 Å for both cases. In these calculations, atomic structure factors are based on the Smith–Burge expression. When the expression of Doyle–Turner is used, the intensity maxima appear at the atom positions when the thickness is 115 ± 5 Å for both cases. The thickness variation of ±10 Å from 105 Å produces the variation of intensity maxima of ±0·2 and ±0·13 Å, respectively, for the cases of Smith–Burge and Doyle–Turner. At the thickness of 105 Å, the amplitudes of the waves of 000, 111 and 200 become nearly the same and thus the contrast of the images of atoms become the highest within the thickness of 170 Å.
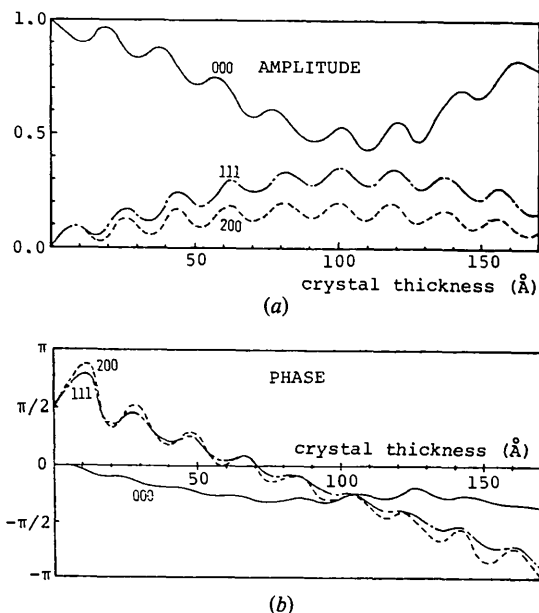
The second condition required to obtain the images of atoms at their correct positions is to avoid the effect of aberrations of the lens which causes the phase change of electron waves. The theoretical resolution limit of the electron microscope used in the present observation is 2·6 Å. Since the spacings of lattice planes of gold {111} and {200} are 2·35 and 2·04 Å, respectively, it seems to be rather difficult to resolve the atom positions in the image when the microscope is operated under normal conditions. Fig. 4 illustrates the two kinds of tilted illumination. In the case of three waves contributing to the image as shown in Fig. 3(a), the undiffracted wave 000 is tilted so that the optical axis is in the center of these three beams 000, 1$\bar{1}$1 and $\bar{1}$11, as shown in Fig. 4(a). In this illumination, all the

Fig. 2. (a) Amplitudes and (b) phases of the seven waves reflected by (000), {111} and {200} of a gold crystal in 01$\bar{1}$ symmetry position as a function of crystal thickness. (Accelerating voltage 100 kV.)
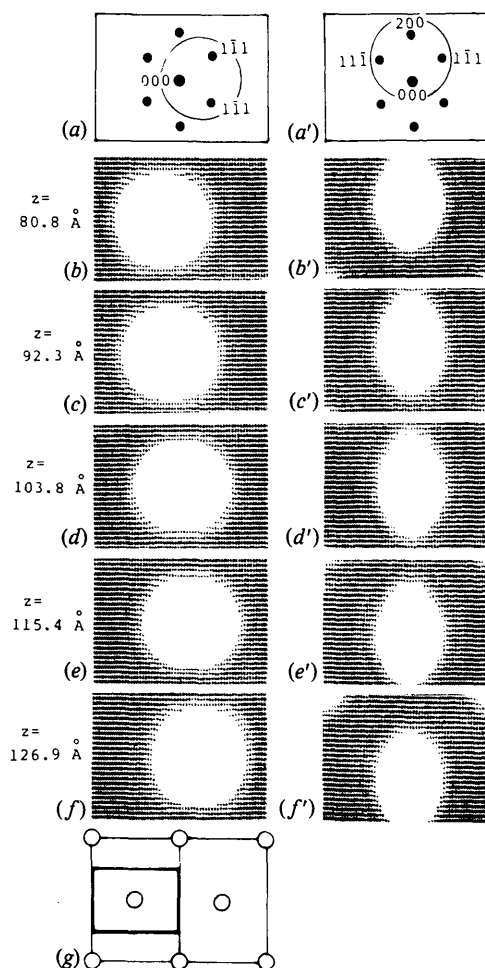

Fig. 3. Thickness dependence of the position of an intensity maximum appearing at the bottom face of a gold crystal in 01$\bar{1}$ symmetry position ($C_s = \Delta f = 0$, 129 beams excited). (a) and (a′) indicate the diffraction patterns. Circles indicate the waves contributing to the intensity at the bottom face. (g) shows the positions of atoms and the area of half-tone pictures in the unit cell.

waves have the same incident angle to the lens axis, and thus the phase shifts of the waves in the lens become the same. Figs. 4(b), (c), (d) and (e) show the calculated images of atoms appearing at the image plane when $C_s = 0.7$ mm and $\Delta f = 700$, 800, 900 and 1000 Å, respectively. As can be seen in these pictures, the image is directly projected onto the image plane with no effect of defocusing. This is because the same phase shift occurs for all waves and it therefore has no influence on the image. When the images are formed by the four waves 000, 200, $1\bar{1}1$ and $11\bar{1}$ as shown in Fig. 3(a'), the incident beam is tilted so that the centre of these waves is on the optical axis as shown in Fig. 4(a'). In this case, the four waves seem to suffer from the different phase change by the lens, because the angle of the 000 and 200 reflections against the optical axis α_1 is different from that of the $1\bar{1}1$ and $11\bar{1}$, α_2. However, they can all have the same phase shift at a certain defocus. When the defocus Δf is $\frac{1}{2}C_s(\alpha_1^2 + \alpha_2^2) = 865$ Å, the phase angles γ_g in (5) of the waves with tilt angles α_1 and α_2 become the same and are given by

$$\gamma_g = -\frac{\pi}{2\lambda} C_s \alpha_1^2 \alpha_2^2. \tag{6}$$

Therefore, 865 Å is the optimum defocus value to obtain the same phase shift for both waves with tilt angles α_1 and α_2. As can be seen in Figs. 4(c') and (d'),

the defocus values of 800 and 900 Å give the images of atoms close to the positions of atoms. The relation between the real part of the contrast transfer function $\cos \gamma$ and the angles α_1 and α_2 are expressed in Fig. 5(a). As is shown by the two arrows, both α_1 and α_2 are in the flat wide band at a defocus of about 800 Å.

This imaging method may be applied to the case of an imperfect crystal containing a twin. The diffraction pattern from the crystal containing a twin is schematically shown in Fig. 5(b). The diffraction spots indicated by suffixes m and t are produced from the matrix and the twin, respectively. In order to obtain the image of the twin structure, at least the five waves in the circle shown in Fig. 5(b) must be included. In order to obtain the image of atoms both in the matrix and the twin at atom positions, these waves must have the same phase after passing through the objective lens. As discussed above, when the optical axis is in the centre of $(000)_{m,t}$, $(200)_m$, $(1\bar{1}1)_m$, $(11\bar{1})_{m,t}$ and the defocus value is 800 Å, the real part of the contrast transfer function becomes as shown in Fig. 5(a) and thus the twin spot $\frac{1}{3}(5\bar{1}1)_t$, whose tilt angle is α_3, appears inside the flat wide band and has nearly the same phase angle as other spots. Therefore, the images of atoms both in the matrix and the twin will appear at the atom positions. Even if a small lattice distortion is at the boundary region, atoms will be reproduced correctly in the image. The defocus, 800 Å, is the optimum focus also for a crystal containing a twin band in this tilted illumination. In the AFF condition in tilted illumination, chromatic aberration can be eliminated more effectively than in axial illumination, because all
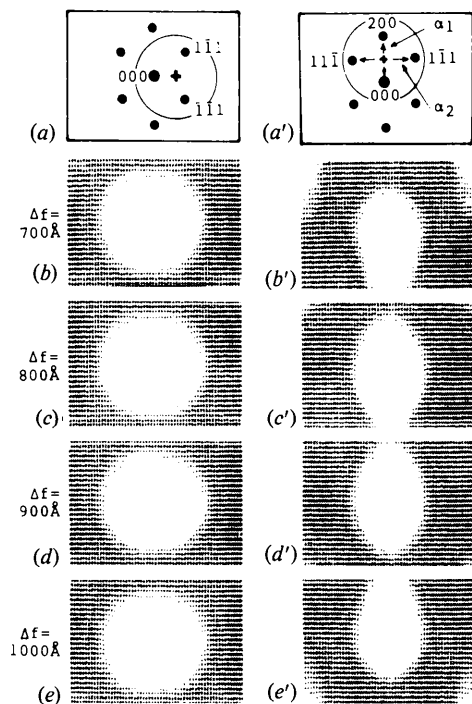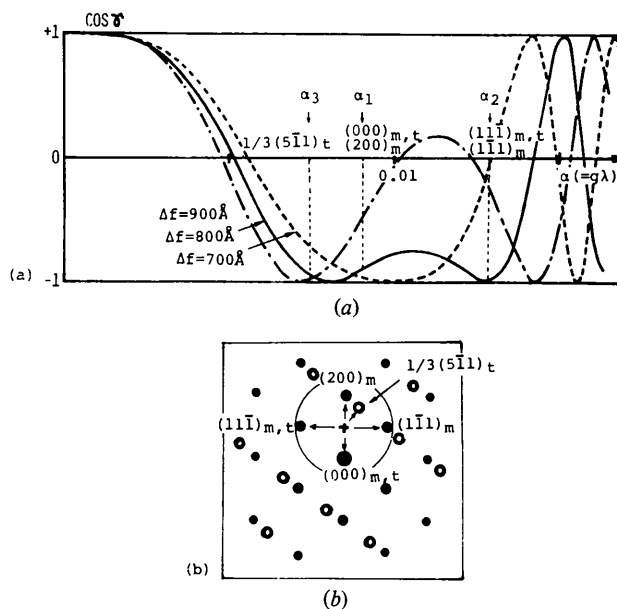
Fig. 4. Defocus dependence of the position of the intensity maximum appearing at the image plane. The $+$ and the circle show the locations of the objective-lens axis and the aperture, respectively. ($C_s = 0.7$ mm, thickness 103.8 Å, 129 beam excited.)

Fig. 5. (a) Real part of the contrast transfer function for $C_s = 0.7$ mm and $\Delta f = 700$, 800 and 900 Å at 100 kV. (b) Electron diffraction pattern of gold in $0\bar{1}\bar{1}$ orientation containing a twin structure. Black and white discs show the diffraction spots from the matrix and the twin respectively.

the waves incident on the electron lens have nearly the same tilt angle to the optical axis.

4. Observation of atoms in gold crystals containing twins and stacking faults

The specimens of gold thin crystals were prepared by vacuum deposition (Pashley, 1959) on a silver single crystal heated at 573 K in a vacuum of 0·13 mPa. By dissolving the substrate silver in nitric acid, gold thin crystals whose surface is parallel to (01̄1) were obtained. The thickness of the gold crystal was measured to be 100 ± 20 Å at the edges of the bent-over regions where the cross section of the crystal can be seen. Observations were carried out with a JEM 120 C electron microscope operated at 100 kV. The spherical aberration coefficient of the objective lens was measured to be 0·7 ± 0·05 mm by using optical diffractograms of the images of thin carbon films (Krivanek, 1976). The images of gold crystals of 01̄1 orientation were photographed by tilting the incident beam so that the centre of the 111, 11̄1, 200 and 000 reflections coincides with the optical axis as shown in Fig. 4(a'). The other reflections were excluded from the image. The direct magnification was 1 300 000 times and the images were photographed with an exposure of about 2 s. Fig. 6 shows an example of an electron-microscope image of a 01̄1 gold crystal containing a twin band, which was photographed with the condition

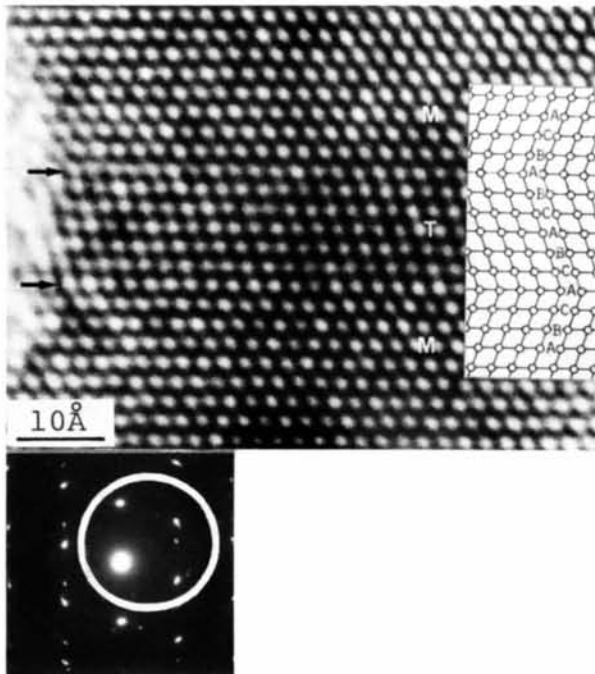shown in Fig. 5(b). Since the incident beam is parallel to [01̄1̄], the coherent twin boundary planes indicated by two arrows are normal to the image plane. Therefore, the change of stacking of atoms from matrix M (ABC stacking) to twin T (ACB stacking) can be seen clearly in the micrograph. Fig. 7 shows a twin band T surrounded by a coherent twin boundary A and a lenticular twin boundary B. In the boundary A, a bright spot contrast anomaly can be seen which was sometimes observed in planar defects; the origin is not yet known. It may be due to the segregation of atoms at the boundary. Fig. 8(a) shows the image of an
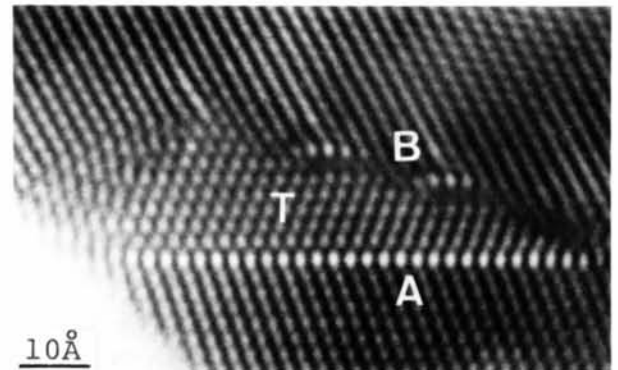

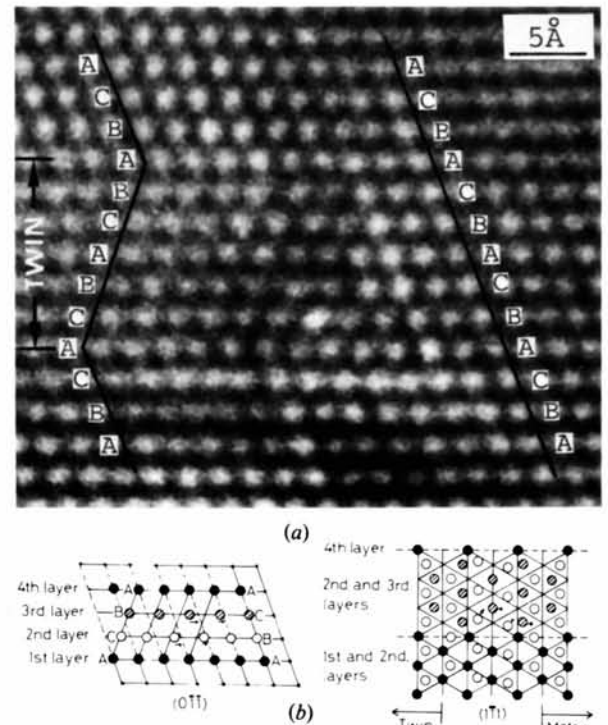Fig. 7. Twin band (T) surrounded by a coherent twin boundary (A) and a lenticular twin boundary (B).

Fig. 6. Image of a gold crystal containing a twin structure together with the corresponding electron diffraction pattern.

Fig. 8. (a) Image of an incoherent boundary at the tip of a twin band. (b) Atomic arrangement estimated from the image in (a) projected to (11̄1) and (01̄1̄).

incoherent twin boundary appearing at a tip of a thin twin plate with a width of six atomic layers. The gradual change of the bright-atom images from ABC stacking in the matrix to ACB stacking in the twin can be seen in the image, as indicated by arrows. A shift of atoms at the tip of the twin band will produce the diffuse scattering of electron waves. They seem to be distributed in the wide band of the contrast transfer function of the objective lens shown in Fig. 5(a) and the phases of electron waves in the diffuse scattering are not changed by the lens, therefore the images of atoms at the tip of the twin band appear at the correct positions. The atomic arrangement in this boundary estimated from the image is shown in Fig. 8(b) as the projections on $(0\bar{1}\bar{1})$ and $(1\bar{1}1)$, where atoms in A, B and C layers are expressed as black, shaded and white circles in the twin band respectively. Figs. 9(a), (b) and (c) show the images of one, two and three stacking faults, respectively. In (a), an intrinsic stacking fault having two partial dislocations indicated by two arrows on both ends of the fault is seen. Near the centre of the stacking fault, some blurred images of atoms can be seen, which may be due to the misarrangement of atoms along $[0\bar{1}\bar{1}]$ and the shape of the contrast transfer function of the objective lens. Using the measured width of the stacking faults, nine atom spacings, the stacking-fault energy was calculated to be 43 mJ m^{-2}. Fig. 9(b) shows the interaction of two intrinsic stacking faults in different slip planes, which produces a sessile dislocation at the intersecting point indicated by an arrow. The reaction process is
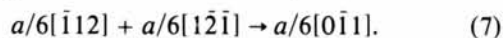
$$a/6[\bar{1}12] + a/6[1\bar{2}\bar{1}] \rightarrow a/6[0\bar{1}1]. \qquad (7)$$

Fig. 9(c) shows three stacking faults in different slip planes which form a Z-shape arrangement of stacking faults by the reaction at the two intersecting points indicated by arrows.

5. Comparison of observations and calculations

Fig. 10 shows the diffraction pattern produced by assuming the large unit cell of $A'B'C'D'$ in Fig. 1. The white and black discs are the diffraction spots from the matrix and the twin, respectively. The small black dots connecting the discs are the pseudo diffraction spots from the structure with the large unit cell. Since large
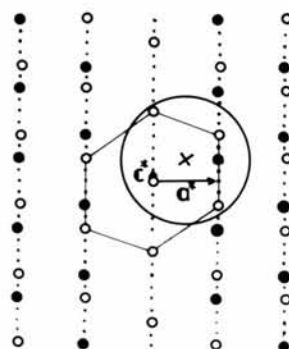

Fig. 10. Diffraction pattern from the crystal with large unit cell $A'B'C'D'$ shown in Fig. 1. White and black discs show the diffraction spots from matrix and twin. The small black dots are the pseudo diffraction spots from the large unit cell.
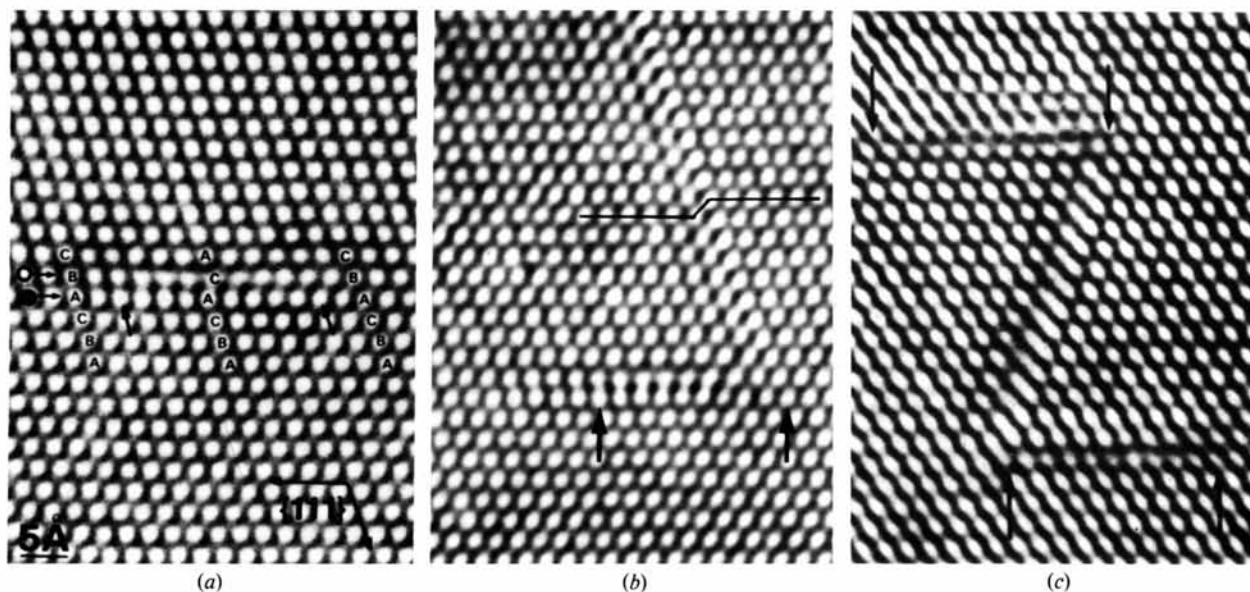

Fig. 9. (a) Image of a stacking fault with accompanying partial dislocations at both ends. (b) Image of two stacking faults in two different slip planes interacting at the intersecting point. (c) Image of three stacking faults interacting at two intersecting points.

unit cells are assumed for the convenience of calculation, the intensities of the small black spots are actually negligible, but must be included for the calculation. In the calculation, 385 waves including pseudo reflections were assumed to be excited in the crystal and 18 waves including pseudo diffraction spots which are indicated in the large circle representing the aperture of objective lens shown in Fig. 10 contribute to the image. The calculated results are shown as half-tone pictures in Fig. 11, together with the experimental results. The variation of the observed contrast is well explained by the calculated results. As can be seen in Fig. 11, the intensity maxima observed
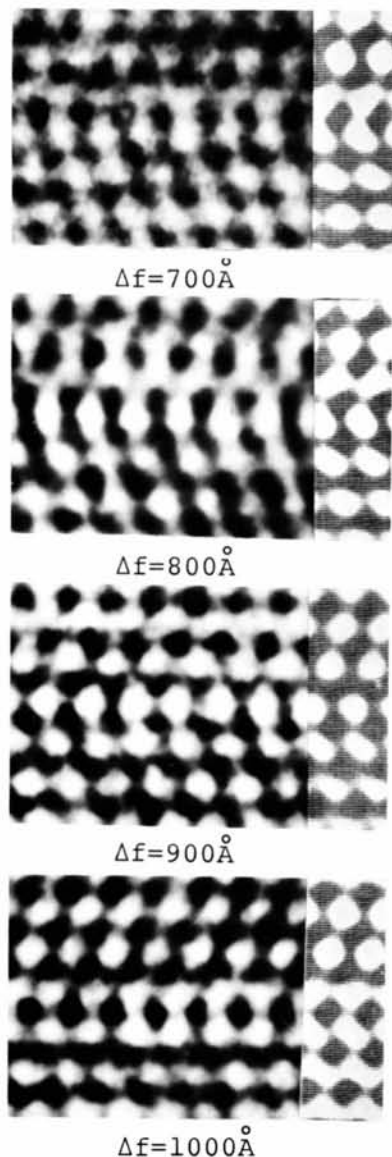
at $\Delta f = 800$ Å appear at the correct positions of the atoms in the crystal, which agrees with the discussions made in the previous section. The positions of the intensity maxima appearing in the matrix and twin at other defocuses do not correspond to atom positions which are arranged symmetrically on either side of the twin boundary.

Figs. 12(a), (b) and (c) show the observed image, the calculated image at a defocus of 800 Å and the model of the intrinsic stacking fault. In the calculation, 485 waves were assumed to be excited in the crystal and 18 waves contributed to the image formation. The location and the size of the objective-lens aperture were the same as those for the case of the coherent twin boundary shown in Fig. 10. Figs. 13(a), (b) and (c) show similar patterns to those shown in Fig. 12 for the extrinsic stacking fault. The positions of the intensity maxima in (a) and (b) agree well with the atom positions in model (c).

6. Conclusion

It has been shown that the phases of the electron waves which are scattered in a gold crystal of $[0\bar{1}\bar{1}]$ orientation by the planes $\{111\}$, $\{200\}$ and (000) become the same at the bottom face of a crystal of 105 Å thickness, and the intensity maxima of the
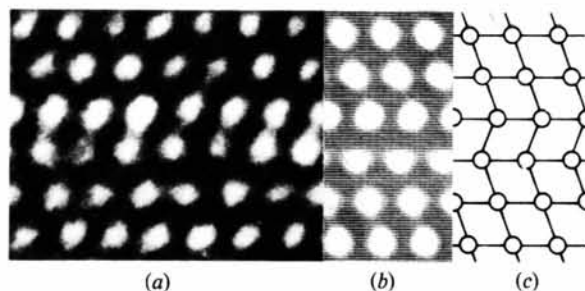

$\Delta f=700$Å

$\Delta f=800$Å

$\Delta f=900$Å

$\Delta f=1000$Å

Fig. 11. Observed and calculated images of a coherent twin boundary for various amounts of defocus. ($C_s = 0.7$ mm, thickness 103·8 Å, 385 waves excited in the crystal and 18 waves contribute to the images.)

(a)   (b)   (c)

Fig. 12. Image of an intrinsic stacking fault. (a) Observed and (b) calculated images. (c) Model. ($C_s = 0.7$ mm, $\Delta f = 800$ Å, 485 waves excited in the crystal and 18 waves contribute to the image.)
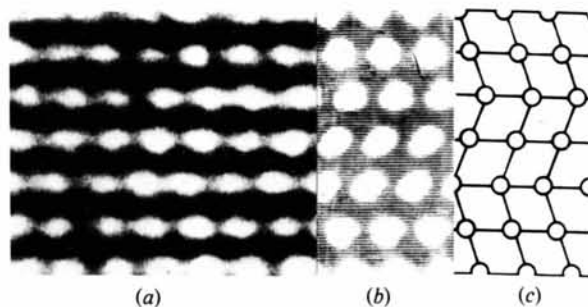

(a)   (b)   (c)

Fig. 13. Image of an extrinsic stacking fault. Conditions are the same as those in Fig. 12.

electron waves appear at the atom positions. It was also shown that the intensity maxima of the electron waves at the bottom face of a gold crystal can be projected onto the image plane without any phase change by the tilted-illumination AFF condition, which is at 800 Å defocus for a lens with spherical aberration coefficient $C_s = 0\cdot 7$ mm at 100 kV. The images photographed with this condition were checked theoretically and experimentally and this confirmed their usefulness for taking the images of atoms at atom positions. This method was applied to observe the images of atoms in gold crystals containing coherent and incoherent twin boundaries and stacking faults.

Fig. 14. Diffraction pattern from a [0$\bar{1}$$\bar{1}$] gold crystal showing the independent waves in the shaded region.

APPENDIX
Reduction of numbers of beams in computing

The simplification of calculation of the contrast utilizing the property of the symmetry of a crystal is described concisely. In order to discuss the problem simply, only the case where the 000, $1\bar{1}1$, $\bar{1}1\bar{1}$, $\bar{1}1\bar{1}$, $11\bar{1}$, 200 and $\bar{2}00$ reflections are excited in a [0$\bar{1}$1] gold crystal is treated. The reflections are labelled 0, 1, 2, 3, 4, 5 and 6, respectively, as shown in Fig. 14. Equation (1) is expressed in matrix representation as

$$\frac{d}{dz}\begin{pmatrix} V_0 \\ \hline V_1 \\ V_2 \\ V_3 \\ V_4 \\ \hline V_5 \\ V_6 \end{pmatrix} = 2\pi i \begin{pmatrix} 0 & a & a & a & a & b & b \\ \hline a & s_1 & b & e & c & a & d \\ a & b & s_2 & c & e & d & a \\ a & e & c & s_3 & b & d & a \\ a & c & e & b & s_4 & a & d \\ \hline b & a & d & d & a & s_5 & f \\ b & d & a & a & d & f & s_6 \end{pmatrix} \begin{pmatrix} V_0 \\ \hline V_1 \\ V_2 \\ V_3 \\ V_4 \\ \hline V_5 \\ V_6 \end{pmatrix}, \quad (A1)$$

where $a = U_{111}/2K$, $b = U_{200}/2K$, $c = U_{022}/2K$, $d = U_{311}/2K$, $e + U_{222}/2K$ and $f = U_{400}/2K$. Since $s_1 = s_2 = s_3 = s_4$ and $s_5 = s_6$ for the crystal whose [0$\bar{1}$1] is parallel to the incident beam, $(A1)$ can be rewritten as the following equivalent equation:

$$\frac{d}{dz}\begin{pmatrix} V_0 \\ V_1 \\ V_5 \end{pmatrix} = 2\pi i \begin{pmatrix} 0 & 4a & 2b \\ a & s_1 + b + c + e & a + d \\ b & 2(a+d) & s_5 + f \end{pmatrix} \begin{pmatrix} V_0 \\ V_1 \\ V_5 \end{pmatrix}. \quad (A2)$$

The V_2, V_3, V_4 and V_6 can be obtained by the relations
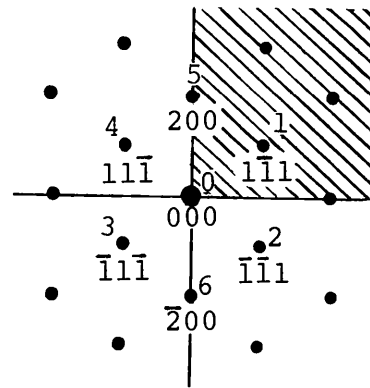
$$V_1 = V_2 = V_3 = V_4, \quad V_5 = V_6. \quad (A3)$$

This simplification is given from the fact that only the waves 000, $1\bar{1}1$ and 200 in the shaded area in Fig. 14 behave independently in the crystal among the seven waves.

References

BOERSCH, H. (1947). Z. Naturforsch. Teil A, **2**, 615–633.
COWLEY, J. M. (1959). Acta Cryst. **12**, 367–375.
COWLEY, J. M. (1975). J. Appl. Cryst. **8**, 204–205.
DOYLE, P. A. & TURNER, P. S. (1968). Acta Cryst. **15**, 390–397.
FUKUHARA, A. (1966). J. Phys. Soc. Jpn, **21**, 2645–2662.
HASHIMOTO, H., ENDOH, H., TAKAI, Y., TOMIOKA, H. & YOKOTA, Y. (1978–79). Chem. Scr. **14**, 23–31.
HASHIMOTO, H., ENDOH, H., TANJI, T., ONO, A. & WATANABE, E. (1977). J. Phys. Soc. Jpn, **42**, 1073–1074.
HASHIMOTO, H., KUMAO, A., ENDOH, H., NISSEN, H.-U., ONO, A. & WATANABE, E. (1975). Proceedings of the EMAG Conference, Bristol, pp. 245–250.
HASHIMOTO, H., SUGIMOTO, Y., TAKAI, Y. & ENDOH, H. (1978). Proc. 9th Int. Congr. on Electron Microscopy, Toronto, Vol. 1, pp. 284–285.
HASHIMOTO, H., TAKAI, Y., YOKOTA, Y., ENDOH, H. & FUKADA, E. (1980). Jpn. J. Appl. Phys. **19**, L1–L4.
HOWIE, A. & WHELAN, M. J. (1961). Proc. R. Soc. London Ser. A, **263**, 217–237.
ISHIDA, Y. & ICHINOSE, H. (1977). High Voltage Electron Microscopy, Proc 5th Int. Conf., Kyoto, Vol. 1, pp. 603–606.
IZUI, K., FURUNO, S., NISHIDA, T. & OTSU, H. (1978–79). Chem. Scr. **14**, 99–108.
KOMODA, T. (1966). Jpn. J. Appl. Phys. **5**, 603–607.
KRIVANEK, O. L. (1976). Optik (Stuttgart), **45**, 97–101.
KRIVANEK, O. L. & MAHER, D. W. (1978). Appl. Phys. Lett. **32**, 451–453.
O'KEEFE, M. A. (1973). Acta Cryst. A**29**, 389–401.
OLSEN, A. & SPENCE, J. C. H. (1979). 37th Ann. Proc. EMSA, Vol. 1, pp. 550–551. Baton Rouge: Claitor.
PASHLEY, D. W. (1959). Philos. Mag. **4**, 324–335.
SCHERZER, O. (1949). J. Appl. Phys. **20**, 20–29.
SMITH, G. H. & BURGE, R. E. (1962). Acta Cryst. **15**, 182–186.